Accepted Manuscript

On the Use of Physical Boundary Conditions for Two-Phase Flow Simulations: Integration of Control Feedback

Mehrez Agnaou, Tanyakarn Treeratanaphitak, Amir Mowla, Marios Ioannidis, Nasser Mohieddin Abukhdeir, Hector Budman

PII: S0098-1354(18)30261-8
DOI: https://doi.org/10.1016/j.compchemeng.2018.08.012
Reference: CACE 6184

To appear in: *Computers and Chemical Engineering*

Received date: 9 April 2018
Revised date: 28 July 2018
Accepted date: 7 August 2018

Please cite this article as: Mehrez Agnaou, Tanyakarn Treeratanaphitak, Amir Mowla, Marios Ioannidis, Nasser Mohieddin Abukhdeir, Hector Budman, On the Use of Physical Boundary Conditions for Two-Phase Flow Simulations: Integration of Control Feedback, *Computers and Chemical Engineering* (2018), doi: https://doi.org/10.1016/j.compchemeng.2018.08.012

Highlights

- The impact of inlet boundary conditions on two-phase flow CFD solutions is studied.
- The two-phase upward flow in a vertical pipe is modeled using the Euler-Euler model.
- Solutions using inlet pressure and velocity Dirichlet boundary conditions differ.
- The gas phase distribution is strongly dependent on the inlet conditions.
- A control scheme is used to enforce the Dirichlet pressure boundary and flow rates.

On the Use of Physical Boundary Conditions for Two-Phase Flow Simulations: Integration of Control Feedback

Mehrez Agnaou[a], Tanyakarn Treeratanaphitak[a], Amir Mowla[a], Marios Ioannidis[a], Nasser Mohieddin Abukhdeir[a,b,*], Hector Budman[a]

[a] *Department of Chemical Engineering, University of Waterloo, 200 University Avenue West Waterloo, N2L 3G1, ON, Canada*
[b] *Department of Physics & Astronomy, University of Waterloo, 200 University Avenue West Waterloo, N2L 3G1, ON, Canada*

Abstract

The sensitivity of two-phase flow simulations using the Euler-Euler model on the inlet boundary conditions is studied. Specifically, the physical relevance of Dirichlet uniform inlet velocity BCs is studied which are widely used due their simplicity and the lack of *a priori* knowledge of the slip velocity between the phases. It is found that flow patterns obtained with the more physically realistic uniform inlet pressure BCs are radically different from the results obtained with Dirichlet inlet velocity BCs, refuting the argument frequently put forward that Dirichlet uniform inlet velocity BCs can be interchangeably used because the terminal slip velocity is reached after a short entrance region. A comparison with experimental data is performed to assess the relevance of the flows obtained numerically. Additionally, a multivariable feedback control method is demonstrated to be ideal for enforcing desired flow rates for simulations using pressure BCs.

Keywords: two-phase flow, computational fluid dynamics, Euler-Euler model, simulations, control

*Corresponding author

1. Introduction

Computational fluid dynamics (CFD) simulation of multiphase flows is a widely used tool for design and optimization of industrial processes. Compared to alternative methods such as scaled-down laboratory experiments, multiphase CFD simulations frequently result in time and cost savings while simultaneously avoiding safety issues inherent to experimental process design. They also yield information about the process which may be expensive or, in many cases, infeasible to determine experimentally. For these reasons and given the increasing accessibility of high-performance computing infrastructure, the use of multiphase CFD in academia and industry is expanding. Examples of multiphase processes in chemical engineering include bubble columns [14, 18], packed-bed and fluidized bed reactors [13], trickle-bed reactors [13, 36], nuclear fuel rod assemblies [7] and hydrocarbon pipelines [12]. Two-phase flows are generally simulated using the two-fluid or Euler-Euler model [11], which uses time-averaging to avoid explicitly capturing the fluid-fluid interface, thereby reducing computational complexity significantly and enabling access to time and length scales relevant to industrial processes. It should be mentioned that different averaging techniques were used in the literature to derive macroscopic momentum and mass conservation equations for two-phase flow [11, 37].

The use of multiphase CFD introduces significant challenges, in addition to benefits. One significant challenge is the approximation of mathematical conditions which, if not addressed appropriately, may offset the advantages of simulation. While this enables simulation of a more simple part of a complex physicochemical process, it introduces another possible source of error through the formulation and imposition of boundary conditions which have differing degrees of physical and numerical relevance. This is especially significant for multiphase flows due to the presence of additional dependent variables such as phase fraction and phase velocities. Appropriate boundary conditions reflect known interactions between the modelled system and the surroundings. Simulation boundary conditions that most faithfully represent the physical reality are generally expensive to evaluate experimentally and may be difficult to implement numerically. Therefore, in practice, coarse approximations for boundary conditions are used which may introduce significant uncertainty with respect to the exact solution and, in some cases, lead to numerical instability.

In multiphase CFD simulations, inlet boundary conditions are typically

the most challenging. Focusing on incompressible two-phase flow simulations using the two-fluid model, the uniform Dirichlet condition for phase velocities at inlets is the most frequently used boundary condition due to its simple formulation and numerical implementation. This boundary condition is, however, inconsistent with the expectations, on physical grounds, of slip velocity between the two phases and no-slip at the intersection of the inlet and walls. The effect of this inconsistency on simulated two-phase flow profiles is hitherto unknown. Nonetheless, this boundary condition is widely used in the literature for simulations of different two-phase flow systems with some recent examples including refs. [4, 17, 21, 42, 43].

Recent experimental research [9, 22, 38] further reinforces the importance of accurate inlet conditions, where it is found that two-phase flow patterns are extremely sensitive to inlet conditions. Liu et al. [22] studied the effect of uniform and non-uniform inlet conditions of vertical air-water two-phase flow in a narrow rectangular duct and found that the velocity profiles across the duct are different with a non-uniform inlet profile compared to an uniform one. Gregorc and Žun [9] found that inlet conditions strongly affected the experimentally-observed bubble size, bubble distribution and flow regime transitions for liquid-gas two-phase flow in microfluidic channels. While the two previous studies focus on gas dispersed in liquid, Yoneda et al. [38] studied steam-water two-phase flow in a large-diameter pipe finding the sensitivity of the distribution of the two phases over the pipe with respect to the inlet conditions.

In summary, despite several experimental studies showing the impact of inlet conditions on the two-phase flow pattern, there exist very few multiphase CFD studies focused on this issue such as refs. [8, 20, 23] (focused on sieve trays). The vast majority of two-fluid CFD studies, the most prevalent in chemical engineering, have used uniform Dirichlet inlet velocity boundary conditions under the assumption that either (i) a physically accurate flow profile will develop after a short entrance region and a terminal slip velocity between phases will be achieved or (ii) the use of the these inlet conditions is an acceptable physical approximation that has no significant impact on the flow pattern. The essence of these assumptions is that there is no significant difference between the solutions obtained with the uniform phase inlet velocity boundary conditions and those obtained with uniform inlet pressure boundary conditions.

In this work, the impact of the inlet boundary conditions on the solutions of two-phase flow problems using the two-fluid model is investigated

for the case of air-water upward dispersed flow in a vertical pipe. The physical relevance of the solutions obtained with inlet Dirichlet uniform velocity boundary conditions are discussed in both cases with and without slip velocity between phases and compared to that obtained with Dirichlet pressure boundary conditions.

However, although the pressure inlet condition is more physically accurate, the use of this boundary condition is not trivial because the velocity distributions for both phases that satisfy desired flow rates with a uniform pressure distribution across the inlet are not known *a priori*. We show in this work that feedback control can be efficiently used to impose desired inlet phase volumetric flow rates. Such approach has been previously followed for imposing one boundary condition in *compressible* two-fluid simulations [24, 25]. We propose in this work the integration of multivariable feedback control into two-fluid CFD simulations in order to enable the use of more consistent Dirichlet pressure inlet boundary conditions under desired volumetric flow rate constraints for each of the two phases.

This paper is organized as follows: first, the background related to the two-fluid model is presented in section 2. Then, the physical problem, the different investigated boundary conditions and the adopted methodology are described in section 3. The simulations results and their comparison to experimental data as well as the control scheme used to set the pressure Dirichlet boundary conditions are presented in section 4. Finally, the conclusions of this work are summarized in section 5.

2. Background

The two-fluid or Euler-Euler model [11] treats phases as inter-penetrating continua where the volume of one phase can not be occupied by the other one and the presence of each one is described by a phase volume fraction. Defining the phase velocity, pressure and time by $\boldsymbol{u}_q$, p and t, respectively, the phase averaged mass and momentum conservation equations are given as follows

$$\frac{\partial(\alpha_q\rho_q)}{\partial t} + \boldsymbol{\nabla}\cdot(\alpha_q\rho_q\boldsymbol{u}_q) = 0, \qquad \text{in} \quad V, \quad \text{(1a)}$$

$$\frac{\partial(\alpha_q\rho_q\boldsymbol{u}_q)}{\partial t} + \boldsymbol{\nabla}\cdot(\alpha_q\rho_q\boldsymbol{u}_q\boldsymbol{u}_q) = \boldsymbol{\nabla}\cdot(\alpha_q\boldsymbol{\sigma}_q) + (\alpha_q\rho_q\boldsymbol{g}) + \boldsymbol{M}_q, \quad \text{in} \quad V, \quad \text{(1b)}$$

where the subscript $q = g, l$ denotes the phase (g is the gas phase and l is the liquid phase), α_q ($\alpha_g + \alpha_l = 1$) is the phase volume fraction and ρ_q

the phase density. In the momentum conservation equation (Eq. 1b), $\boldsymbol{\sigma}_q$ is the phase stress tensor that includes both the viscous and Reynolds stress tensors, $\boldsymbol{g} = -g\boldsymbol{e}_z$ is the gravitational acceleration and $\boldsymbol{M}_q$ is the inter-phase momentum transfer term which results from the averaging procedure. The inter-phase momentum transfer term can be decomposed into different terms depending on their origin as follows [5, 37]

$$\boldsymbol{M}_q = \boldsymbol{F}_{drag} + \boldsymbol{F}_{lift} + \boldsymbol{F}_{vm}, \quad q = g, l, \tag{2}$$

where $\boldsymbol{F}_{drag}$, $\boldsymbol{F}_{lift}$ and $\boldsymbol{F}_{vm}$ represent the drag, lift and virtual mass contributions to the momentum transfer term, respectively. The drag term has the most important effect [37] on the inter-phase momentum transfer term, hence, the choice of the drag model has a significant impact on simulation results [2, 32, 40]. The drag effect is modeled by means of a mixture model that is assumed valid for the whole range of volume fractions in the two-phase system as follows [37]

$$\boldsymbol{F}_{drag} = \frac{3}{4}\alpha_a\alpha_b\left[\left(\alpha_a\frac{C_{da}\rho_b}{d_a}\right) + \left(\alpha_b\frac{C_{db}\rho_a}{d_b}\right)\right]\|\boldsymbol{u}_r\|\boldsymbol{u}_r, \quad a, b = g, l, \qquad a \neq b, \tag{3}$$

where C_{da} and C_{db} are the drag coefficients of phases a and b, respectively and $\boldsymbol{u}_r = \boldsymbol{u}_b - \boldsymbol{u}_a$ is the relative velocity. The diameter of the particles of phases a and b are d_a and d_b, respectively. d_g is the gas bubble diameter and d_l is the liquid droplet diameter. The Tomiyama empirical correlation of the drag coefficient [34], generally applicable for slightly contaminated gas-liquid systems, is used and is given as follows

$$\begin{aligned} C_{da} &= \max\left\{\min\left[\frac{24}{Re_a}(1 + 0.15Re_a^{0.687}), \frac{72}{Re_a}\right], \left[\frac{8}{3}\frac{Eo_a}{Eo_a + 4}\right]\right\}, \\ Eo_a &= \frac{g(\rho_b - \rho_a)d_a^2}{\sigma_{g,l}}, \qquad a, b = g, l, \\ Re_a &= \frac{d_a\|\boldsymbol{u}_r\|}{\nu_b}, \qquad a \neq b, \end{aligned} \tag{4}$$

where $\sigma_{g,l}$ is the gas-liquid interface surface tension, Eo_a is the Eötvös number of phase a and represents the ratio of buoyancy to surface tension force, ν_b is the kinematic viscosity of phase b and Re_a is the Reynolds number. The

lift contribution to the momentum transfer term, $\boldsymbol{F}_{lift}$, in Eq. 2 is given as follows [37]

$$\boldsymbol{F}_{lift} = \alpha_a \alpha_b (\alpha_b C_{la} \rho_b + \alpha_a C_{lb} \rho_a) \boldsymbol{u}_r \times \boldsymbol{\nabla} \times (\alpha_a \boldsymbol{u}_a + \alpha_b \boldsymbol{u}_b), \quad a, b = g, l, \quad a \neq b, \tag{5}$$

where C_{la} and C_{lb} are respectively the lift coefficients for phases a and b. Few studies have attempted to quantify the lift coefficient and the lift force is often either neglected or a value for the lift coefficient is assumed [15, 16, 26]. The lift force governs the transverse movement of the dispersed phase in a fluid and has a perpendicular direction with respect to the flow direction [1, 31, 35]. As in the considered flow configurations the transverse movement of the fluids is negligible compared to the main flow and as the lift contribution to the inter-phase momentum transfer term is minor compared to the drag, the lift force was neglected. The virtual mass force that occurs when one phase accelerates with respect to the other is modeled in the same way as the drag contribution. The mixture model is assumed to be valid for the whole range of phase volume fractions. Accordingly, the virtual mass force is given by

$$\begin{aligned} \boldsymbol{F}_{vm} = \alpha_a \alpha_b (\alpha_b C_{vma} \rho_b + \alpha_a C_{vmb} \rho_a) \Bigg[& \left(\frac{\partial \boldsymbol{u}_b}{\partial t} + \boldsymbol{u}_b \cdot \boldsymbol{\nabla} \boldsymbol{u}_b \right) \\ & - \left(\frac{\partial \boldsymbol{u}_a}{\partial t} + \boldsymbol{u}_a \cdot \boldsymbol{\nabla} \boldsymbol{u}_a \right) \Bigg], \end{aligned} \qquad a, b = g, l, \quad a \neq b, \tag{6}$$

where C_{vma} and C_{vmb} are the virtual mass coefficients for phases a and b, respectively. The virtual mass coefficients are treated in the same manner as the lift ones. A constant value of 0.5 is often assumed [31] for both C_{vma} and C_{vmb}.

3. Methods

3.1. Initial Boundary Value Problem

The example multiphase process used in this work is two-phase flow of two immiscible, incompressible, Newtonian fluids in a vertical cylindrical pipe with height $H = 1.5$ m and diameter $D = 15$ cm under isothermal conditions ($T = 293.15$ K). The lower, upper and lateral boundaries are referred to as inlet, outlet and wall, respectively (Fig. 1). The two considered fluids are air (g) and water (l) and their physical properties are shown in Table 1.

Constant physical properties are assumed for both phases corresponding to $T = 293.15$ K and $p = 101325$ Pa.

The initial and boundary conditions for the conservation of mass and momentum equations (Eqs. 1) are:

$$\boldsymbol{u}_q(\boldsymbol{x}, 0) = \boldsymbol{0}, \tag{7a}$$

$$p(\boldsymbol{x}, 0) = 0, \tag{7b}$$

$$\alpha_g(\boldsymbol{x}, 0) = 0.15, \qquad \alpha_l(\boldsymbol{x}, 0) = 1 - \alpha_g, \tag{7c}$$

$$\boldsymbol{u}_q(\boldsymbol{x}, t) = \boldsymbol{0}, \qquad \text{on wall,} \tag{7d}$$

$$\begin{aligned} &\boldsymbol{\nabla_n} p(\boldsymbol{x}, t) = \boldsymbol{0}, \\ &\boldsymbol{\nabla_n} \alpha_q(\boldsymbol{x}, t) = \boldsymbol{0}, \end{aligned} \qquad \text{on wall,} \qquad q = g,\, l, \tag{7e}$$

$$p(\boldsymbol{x}, t) = p^{outlet}, \qquad \text{on outlet,} \tag{7f}$$

$$\begin{aligned} &\boldsymbol{\nabla_n} \boldsymbol{u}_q(\boldsymbol{x}, t) = \boldsymbol{0}, \\ &\boldsymbol{\nabla_n} \alpha_q(\boldsymbol{x}, t) = \boldsymbol{0}, \end{aligned} \qquad \text{on outlet,} \qquad q = g,\, l, \tag{7g}$$

where the two phases are initially static (Eqs. 7a-7b) and forming a dispersion of 15% gas (Eqs. 7c) It must be mentioned here that different initial conditions were tested and the same solution, in terms of time averaged profiles, was obtained. At the wall boundary, a no-slip velocity boundary condition (Eq. 7d) is imposed in addition to the Neumann zero normal gradient boundary condition for both the pressure and phase fractions (Eqs. 7e), where $\boldsymbol{n}$ is the unit outward normal to the surface. At the outlet, a Dirichlet pressure boundary condition is enforced (Eq. 7f) and the Neumann zero normal gradient boundary condition is imposed for the velocity and phase fractions (Eqs. 7g). Three different inlet boundary conditions were tested in order to investigate their impact on the resulting flow pattern:

Case I: velocity Dirichlet boundary condition with no gas-liquid slip velocity (Eqs. 8a)

Case II: pressure Dirichlet boundary condition (Eqs. 8b)

Case III: velocity Dirichlet boundary condition with gas-liquid slip (Eqs. 8c)

These boundary conditions are formulated, respectively, as:

$$\begin{aligned} &\boldsymbol{u}_q = \boldsymbol{u}_q^{inlet}, \\ &\boldsymbol{u}_g^{inlet} = \boldsymbol{u}_l^{inlet}, \\ &\alpha_q = \alpha_q^{inlet}, \end{aligned} \qquad \text{on inlet,} \qquad q = g, l, \tag{8a}$$

$$\begin{aligned} &p = p^{inlet}, \\ &\alpha_q = \alpha_q^{inlet}, \end{aligned} \qquad \text{on inlet,} \qquad q = g, l, \tag{8b}$$

$$\begin{aligned} &\boldsymbol{u}_q = \boldsymbol{u}_q^{inlet}, \\ &\boldsymbol{u}_g^{inlet} = S_{g-l}\boldsymbol{u}_l^{inlet}, \\ &\alpha_q = \alpha_q^{inlet}, \end{aligned} \qquad \text{on inlet,} \qquad q = g,\ l, \tag{8c}$$

where S_{g-l} is the gas-liquid slip velocity ratio.

Case I, the velocity Dirichlet boundary condition without gas-liquid slip velocity (Eqs. 8a), is the most widely used due to its simplicity of numerical formulation and implementation. It was stated in ref. [21] that despite its artificial imposition of zero slip velocity between the phases, the uniform velocity condition is a valid approximation in that the velocity profiles will develop such that slip velocity between the phases is obtained after a short entrance region. When this boundary condition is used, uniform gas and liquid velocity profiles are imposed at the inlet and $\boldsymbol{u}_g^{inlet} = \boldsymbol{u}_l^{inlet}$ as the gas-liquid slip velocity is not known *a priori*. The two fluids enter the domain in the direction normal to the inlet boundary and thus, only the z-component of the inlet velocity vector fields is non-zero, $\left\|\boldsymbol{u}_g^{inlet}\right\| = u_{gz}^{inlet} = \left\|\boldsymbol{u}_l^{inlet}\right\| = u_{lz}^{inlet}$. The velocity value is determined from the operating total volumetric flow rate, $\boldsymbol{u}_g^{inlet} \cdot \boldsymbol{n} = \boldsymbol{u}_l^{inlet} \cdot \boldsymbol{n} = -Q_T^{inlet}/A$ where $A = \pi D^2/4$ is the inlet cross-sectional area and $\boldsymbol{n}$ the unit outward normal. The total flow rate is given by the sum of the gas and liquid flow rates as follows

$$Q_T^{inlet} = Q_g^{inlet} + Q_l^{inlet} = -\int\limits_{inlet} \alpha_g \boldsymbol{u}_g \cdot \boldsymbol{n} \mathrm{d}s - \int\limits_{inlet} (1-\alpha_g)\boldsymbol{u}_l \cdot \boldsymbol{n} \mathrm{d}s, \tag{9}$$

where Q_g^{inlet} and Q_l^{inlet} are the gas and liquid volumetric flow rates, respectively and ds refers to a surface element. The inlet gas volume fraction of

Eqs. 8a is given by $\alpha_g^{inlet} = Q_g^{inlet}/Q_T^{inlet} = Q_g^{inlet}/(Q_g^{inlet} + Q_l^{inlet})$.

In case II, the pressure Dirichlet boundary condition is given by Eqs. 8b. A uniform pressure field is imposed at the inlet boundary which corresponds to the assumption that the outlet flow of the pump being unidirectional. The physical justification of this condition is obvious, at least in the dispersed flow regime, where no important velocity variation with respect to the mean flow is expected to occur and alter the uniformity of the pressure field across each cross-section of the pipe. The benefit of this boundary condition compared to the uniform velocity boundary condition is that the gas-liquid slip velocity at the inlet is present, it allows for the development of non-uniform flow profiles consistent with the model governing equations and it satisfies the zero velocity condition at the wall. Imposing this condition is achieved through determining values of p^{inlet} and α_g^{inlet}, unknown *a priori*, to satisfy desired gas and liquid volumetric flow rates. This condition is enforced in this work by means of a multivariable control procedure described in section 4.3.

Case III, velocity Dirichlet boundary condition with slip between the two phases (Eqs. 8c) requires *a priori* knowledge of the gas-liquid slip velocity but, as with case I, assumes a uniform velocity profile within the inlet. The gas-liquid slip velocity ratio S_{g-l} is obtained from the simulation using case II and consequently, it also requires the use of the feedback control scheme. Although not strictly physical, the purpose of investigating this variation of the velocity Dirichlet boundary condition is to assess whether or not it is possible to obtain a flow pattern similar to the one obtained with case II by imposing the correct slip velocity between the two phases.

3.2. Simulation Conditions

The partial differential equation system under consideration consists of Eqs. 1, Eqs. 7 and (individually) each of the inlet boundary conditions of Eqs. 8. The model was solved numerically using the `multiphaseEulerFoam` solver of the open-source CFD toolbox `OpenFOAM` [33].

Two different flow configurations were considered in order to investigate the impact of increasing the gas flow rate on the resulting flow structure. Whereas one total volumetric flow rate was adopted for the two configurations, $Q_T^{inlet\,set} = 6 \times 10^{-4}$ m^3/s, the gas flow rate was varied as follows:

Configuration A: a gas flow rate of $Q_g^{inlet\,set} = 0.3 Q_T^{inlet\,set} = 1.8 \times 10^{-4}$ m^3/s corresponding to gas and liquid superficial velocities, respectively, $u_{gs} = Q_g^{inlet\,set}/A \approx 0.0102$ m/s and $u_{ls} = Q_l^{inlet\,set}/A \approx 0.02377$ m/s

Configuration B: a gas flow rate of $Q_g^{inlet\,set} = 0.5Q_T^{inlet\,set} = 3 \times 10^{-4}$ m^3/s corresponding to gas and liquid superficial velocities, respectively, $u_{gs} = Q_g^{inlet\,set}/A \approx 0.017$ m/s and $u_{ls} = Q_l^{inlet\,set}/A \approx 0.017$ m/s

The computational domain (Fig. 1) was meshed using hexahedral elements and mesh-independent (converged) numerical solutions where determined through a sensitivity analysis of the solution to the number of elements (Fig. 2). This analysis was carried out using case I inlet conditions and configuration A of flow rates and the gas hold up $\overline{\langle \alpha_g \rangle^V}$ was used as the basis for comparison. This quantity corresponds to the time-average over the fully-developed flow interval (FDFI) of the volume-averaged gas volume fraction. It is given by

$$\overline{\langle \alpha_g \rangle^V} = \frac{\int_{FDFI} \langle \alpha_g \rangle^V \, \mathrm{d}t}{\int_{FDFI} \mathrm{d}t}, \tag{10}$$

where the volume averaged gas volume fraction is

$$\langle \alpha_g \rangle^V = \frac{\int_V \alpha_g \mathrm{d}v}{\int_V \mathrm{d}v}, \tag{11}$$

and $\mathrm{d}v$ is an elementary volume.

Fig. 2 shows that mesh-independence is achieved after 50000 elements. Increasing the number of grid blocks 8 times leads to a relative error on the gas hold up, $\overline{\langle \alpha_g \rangle^V}$, of less than 0.32%. Thus, the mesh adopted in this work comprises of 137592 elements as a trade-off between acceptable accuracy and computation time. The number of cells across the cylinder's diameter is 28.

4. Results and Discussion

4.1. Inlet Conditions Effects on Hydrodynamics

4.1.1. Phase Distribution

Simulations were performed of the air-water upward pipe flow process using inlet conditions corresponding to cases I-III (Eqs. 8) and configurations A and B in order to determine their effects on multiphase hydrodynamics.

Fully-developed flow phase distribution for each of the cases and configurations are shown in Figs. 3-6. The significantly differing flow patterns resulting from the same simulation conditions, with the sole difference being inlet conditions, highlight the sensitivity of the solution of the two-phase flow problem to the inlet boundary condition used to induce the flow.

The dispersed flow regime in co-current gas-liquid two-phase systems was found from experiments reported in the literature to be characterized by almost uniformly distributed bubbles, and no bubble coalescence and breakup. Therefore, a narrow bubble size distribution was observed and the gas holdup was reported to be radially uniform in this flow regime [19, 28, 29].

For air-water systems at ambient conditions, Zhang et al. [41] proposed a flow map diagram based on the values of gas and liquid superficial velocities in a column of 0.0826 m diameter. According to Zhang et al. [41], dispersed and discrete flow regimes are both characterized by uniformly sized bubbles, with slightly larger bubbles in the latter. From the diagram reported in the latter reference, dispersed flow regime occurs while the superficial gas velocity is less than 0.04 m/s regardless of the liquid superficial velocity. Hyndman et al. [10] also reported observation of dispersed flow regime in superficial velocities of up to 0.04 m/s in a column of 0.2 m diameter. Fair [6] and Schumpe and Grund [27] stated that dispersed flow regime prevails in systems with superficial velocities of less than 0.05 m/s. In this work, the pipe diameter is $D = 0.15$ m and the adopted superficial gas and liquid velocities are always less than 0.024 m/s. Therefore, according to the cited experimental studies, the occurrence of the dispersed flow regime in the vertical cylindrical pipe and hydrodynamic behavior similar to that of Zhang et al. [41] are expected.

Focusing on case I inlet conditions, velocity Dirichlet boundary conditions without gas-liquid slip, simulation results for this case, shown in Figs. 3 and 5, correspond to gas-rich rising columns whose morphology varies in time. It must be emphasized that this flow morphology persists up to a distance equivalent to ten times the diameter of the entrance of the domain (simulation domain length) and is enhanced as distance from the inlet increases. As shown in Figs. 3 and 5, simulations using case I inlet conditions result in a fully-developed flow that is exhibits periodic large amplitude velocity fluctuations as different instantaneous gas-liquid distributions are observed.

This result may indicate that lateral forces, such as lift, might be important and, hence, cannot be neglected. In order to investigate the effect of the lift force on the flow pattern, we performed an additional simulation with case I inlet conditions for flow configuration B modeling lift force. The two-

phase problem was solved using the `twoPhaseEulerFoam` solver of the CFD toolbox `OpenFOAM` [33]. The Tomiyama lift closure model [35] was considered. The flow resulting from this simulation was similar to the one reported on Figs. 5 for the simulation where lift force was neglected. Thus, neglecting lift force for the flow configurations under study, where the velocity field around the bubbles with respect to the bubble's axis parallel to the pipe is quasi-symmetric, has only a marginal effect on the resulting flows. Moreover, it should be mentioned that modeling lift is still under debate as no well-accepted closure model is available in the literature [31, 32]. Additionally, the lift coefficient is often used as a tuning parameter to improve the agreement between simulation and experimental results and does not necessarily reflect the actual physics of the system [31].

Simulation results for cases II-III inlet conditions, pressure Dirichlet conditions and velocity Dirichlet with gas-liquid slip velocity, are shown in Figs. 4 and 6 for configurations A and B, respectively. These simulation results differ significantly from case I in that a homogeneous distribution of the gas and liquid phases is observed, for both cases II and III. In order to quantitatively analyze and compare gas volume fractions for simulations results, histograms of the time-averaged portions of the computational domain (*i.e.*, the pipe of Fig. 1) over the fully-developed flow interval (FDFI) $\overline{V_\alpha/V}$,

$$\overline{V_\alpha/V} = \frac{\int_{FDFI} V_\alpha/V \, \mathrm{d}t}{\int_{FDFI} \mathrm{d}t}, \tag{12}$$

corresponding to the different gas volume fraction α_g intervals were computed, shown in Figs. 7 and 8. The portion of the computational domain containing a dispersion of a gas volume fraction within the ith interval $[\alpha_{g,i}, \alpha_{g,i+1}]$ is given by

$$V_\alpha/V = \frac{\int_{\alpha_g \in [\alpha_{g,i}, \alpha_{g,i+1}]} \mathrm{d}v}{V}. \tag{13}$$

For configuration A (see Fig. 7), the distribution of α_g for case I, ranging from $\alpha_g = 0$ to 0.1088 is significantly broader compared to those of cases II

and III, which are highly localized. Indeed, whereas cases II and III lead to values of $\alpha_g \in [0.0335, 0.0419]$ occupying, respectively, 98.93% and 100% of the volume of the pipe, only 64.16% of the computational domain corresponds to this α_g interval with case I inlet conditions. The remaining 26.73% and 9.1% portions of the domain for case I contain values of $\alpha_g \in [0, 0.0335]$ and $\alpha_g \in [0.0419, 0.1088]$, respectively. It should be emphasized that the gas-rich rising columns observed with the case I inlet conditions on Fig. 3 correspond to values of $\alpha_g \in [0.0419, 0.1088]$ and occupy up to 9.1% of the volume of the pipe.

The analysis of the histogram corresponding to configuration B (see Fig. 8) shows, as for configuration A, a highly localized distribution of the gas volume fraction α_g with cases II and III inlet conditions and confirms the phase distribution observations of Figs. 3-6. In fact, cases II and III have, respectively, 74.85% and 100% of the volume of the pipe containing a dispersion of $\alpha_g \in [0.0480, 0.0640]$ whereas only 35.69% of the pipe's volume corresponds to this α_g interval of values with case I inlet conditions. Moreover, compared to configuration A, increasing the gas flow rate results with case I inlet conditions in a broader distribution of α_g, ranging from $\alpha_g = 0$ to 0.21, and in gas-rich rising columns of relatively higher α_g. Configuration B (Fig. 8) shows also, as for configuration A, a quasi-homogeneous phase distribution with case III inlet conditions whereas cases I and II present a certain heterogeneity. Indeed, 32.94% and 5.79% of the computational domain volume contain a dispersion of $\alpha_g \in [0, 0.0480]$, respectively, for cases I and II inlet conditions. The remaining 31.37% and 19.36% of the pipe's volume, corresponding respectively to cases I and II, presents a dispersion of $\alpha_g \in [0.064, 0.21]$ with the solution obtained using the velocity Dirichlet boundary conditions (*i.e.*, inlet boundary condition case I) showing volume portions with the highest α_g values.

4.1.2. Velocity Profiles

The velocity profiles obtained with the three different inlet conditions cases and the flow rate configurations A and B are analyzed in this section. Figures 9 and 10 correspond, respectively, to configurations A and B and show the time-averaged gas and liquid velocity profiles over the fully-developed flow interval considered in the simulations. These profiles were plotted at half-pipe height, $z = 0.75$ m, along an arbitrary radial direction from the center of the pipe to the wall in order to ensure a minimum impact from the inlet and outlet boundaries.

Figure 9 shows that the gas velocity profiles obtained for each of the three inlet conditions cases are generally similar to each other and present a flat shape on a large part far from the wall. Near the pipe's wall, where no-slip velocity boundary conditions are imposed, velocity profiles obtained with case II and case III inlet conditions present a sharp angle, whereas a smoother transition from zero velocity to the flat profile is observed for the case I inlet conditions. A similar behavior is reported for the liquid velocity profiles where the three inlet conditions cases result in comparable profiles with a large flat part at the center of the pipe and different shapes near the wall (*i.e.*, at high values of y). In particular, a non-negligible liquid backflow occurs with case I inlet conditions at $y \geq 0.068$ m as indicated by negative velocity values while profiles corresponding to cases II and III inlet conditions show smooth shapes with positive velocities. It must be highlighted here that the occurrence of the backflow is considered physical as the same hydrodynamics were observed in both experimental [30, 39] and numerical works [30, 32] on comparable two-phase systems.

On the other hand, when higher gas flow rate is considered (see Fig. 10 corresponding to flow rate configuration B), the differences between velocity profiles obtained for each of the three inlet conditions cases become more significant. For example, from Fig. 10, the gas velocity profile for the case I inlet conditions is parabolic unlike the ones for cases II and III that present a flat shape at the central region of the pipe. Near the wall, the gas velocity profile for the case III inlet conditions presents a sharp angle as observed before on configuration A while for case II, a smoother shape can be seen. A parabolic profile for case I inlet conditions and a profile with a flat shape region at the center of the pipe for cases II and III is also observed for the liquid velocity. Furthermore, as for configuration A, a non-negligible liquid backflow develops near the wall for case I inlet conditions. A less pronounced liquid backflow can also be seen for case II inlet conditions for the flow conditions of configuration B.

The analysis of the velocity profiles carried out here highlights their sensitivity to the inlet conditions. At low gas flow rate, similar profiles are observed with the exception that liquid backflow occurs with inlet Dirichlet velocity boundary condition. At high gas flow rates, the velocity profiles significantly differ. The velocity Dirichlet boundary condition with slip velocity (*i.e.*, case III inlet conditions) leads to velocity profile shapes quasi-insensitive to the change in gas flow rate adopted here and to plug-flow like profiles. The velocity profiles reflect the different phase distributions over

the computational volume depending on the inlet conditions case observed in section 4.1.1. The shapes of these profiles result from the structure of the flow, discussed in the section 4.1.3.

4.1.3. Flow Structure

The phase distribution depends on the flow structure. In order to understand the mechanisms that lead to the appearance of different distributions, the structure of the flow was analyzed qualitatively and quantitatively from the streamlines. The instantaneous gas and liquid streamlines over a longitudinal cross section of the pipe, along its symmetry axis, are shown on Figs. 11-14.

From Figs. 11 and 13, respectively corresponding to configurations A and B, the gas streamlines are quasi-straight for the different inlet conditions cases with some distortions that appear at high gas flow rate (Fig. 13). On the other hand, liquid streamlines of Figs. 12 and 14 show distortions of different intensities as a function of the inlet boundary case. The liquid flow structure obtained with case III inlet conditions is characterized by straight liquid streamlines (see Figs. 12c and 14c). This can explain the fact that the phase distribution observed with this inlet conditions case is more homogeneous as compared to the other two cases. The liquid flow structures corresponding to cases I and II inlet conditions show distortions that become stronger and give rise to traveling vortices as the gas flow rate increases. It should be noted, however, that the liquid flow streamlines for case I inlet conditions appear to be more distorted than the ones for case II. This may explain why the phase distribution for case I inlet conditions is significantly broader compared to those of cases II and III.

In order to quantify the structure of the liquid streamlines, that are found more sensitive with respect to the inlet condition, the liquid flow tortuosity, T, was computed. Tortuosity characterizes the length of the flow paths with respect to the main flow and different definitions were proposed in the literature [3]. In this work, the following definition, based on the liquid velocity volume averages, was used

$$T = \frac{\langle |\boldsymbol{u}_l| \rangle^V}{\langle u_{lz} \rangle^V} \geq 1, \tag{14}$$

where $\langle |\boldsymbol{u}_l| \rangle^V$ and $\langle u_{lz} \rangle^V$ are, respectively, volume averages of the liquid velocity magnitude and the velocity component aligned with the main flow

direction (*i.e.*, along the z-axis). It should be noted here that the volume averages were computed in the same way as in Eq. 11. The advantage of the tortuosity definition of Eq. 14 compared to the classical ones proposed in the literature, that are based on the streamline length [3], lies in the fact that the computation of the flow streamlines is not required. From Eq. 14, T is equal to unity for streamlines perfectly aligned with the z-axis. As the streamlines become more tortuous, T increases.

The time-averaged tortuosity over the fully-developed flow interval, $\overline{T}$, given by

$$\overline{T} = \frac{\int\limits_{FDFI} T \mathrm{d}t}{\int\limits_{FDFI} \mathrm{d}t}, \tag{15}$$

was computed for all the simulation results corresponding to the different inlet conditions cases and flow rate configurations. Values of $\overline{T}$ are reported on Tab. 2 and they further strengthen the observation that the solution of the two-phase flow problem depends strongly on the inlet boundary condition. In fact, values of $\overline{T}$ differ significantly from one inlet conditions case to another.

For the flow obtained with case III inlet conditions, $\overline{T} = 1$ for both configurations A and B (see Tab. 2). This is consistent with the flow visualizations of Figs. 12c and 14c) as the streamlines are quasi-straight. Tortuosity values for case II inlet conditions, $\overline{T} = 1.31$ and 3.83 respectively for configurations A and B, are larger than the ones for case III and approximately twice smaller than the ones for case I. This indicates that the liquid flow paths are longer for case I compared to cases II and III and that the ones for case II are longer than those for case III thus confirming the flow analysis of Figs. 11-14.

The differences in tortuosity highlight the correlation between the flow structure and the phase distribution. It is found that the higher the flow tortuosity is, the broader the phase distribution is. In the extreme case of quasi-straight streamlines and a tortuosity close to unity, as for the two-phase flow solution with case III inlet conditions, a quasi-perfectly homogeneous phase distribution is observed. The disturbances that appear in the velocity fields lead to distorted and tortuous flow streamlines, the formation of vortices and to an heterogeneous phase distribution. These disturbances are attributed to the mechanisms of acceleration and deceleration of gas and

liquid fluid particles relative to each other that occur in order to establish the physical slip velocity when the non-physical inlet boundary condition is used. In situations involving heat and mass transfer, significant differences in the tortuosity of flow structures may be expected to have measurable implications.

4.2. Experimental Validation

Two-phase gas-liquid experiments were performed with the purpose of providing a basis for further qualitative validation of the simulation results. The experimental conditions replicate the simulation conditions described in 4.1.1. The experimental gas-liquid flow system used in this study is depicted in Figure 15. The setup is a cold-flow pilot scale reactor which consists of two regions, the gas-liquid distributor (plenum chamber) at the bottom and the test section. A column made of clear PVC pipe with an inner diameter of 15.2 cm and a total height of 1.7 m, was used. The plenum chamber has the same diameter as the column and is 20 cm in height. A perforated plate containing 3 mm circular holes is sandwiched between the test section and the plenum chamber. This plate is designed to evenly distribute gas and liquid within the column. Air and distilled water are used as the working fluids in these experiments.

Two sets of experiments were performed according to flow configurations adopted in this work:

A) $Q_g^{inlet\,set} = 0.3 Q_T^{inlet\,set} = 1.8 \times 10^{-4}$ m^3/s ($u_{gs} \approx 0.0102$ m/s and $u_{ls} \approx 0.02377$ m/s)

B) $Q_g^{inlet\,set} = 0.5 Q_T^{inlet\,set} = 3 \times 10^{-4}$ m^3/s ($u_{gs} \approx 0.017$ m/s and $u_{ls} \approx 0.017$ m/s).

A Canon EOS 550D (f/4; 1/1000 s; ISO 3200) digital camera was used for taking images in the developed region of the two-phase upward flow ranging from 1.1 m to 1.3 m above the distributor plate.

Figure 16 shows the flow patterns observed for each flow rate configuration. For both considered flow rates, the bubbles are primarily uniformly distributed across the cross-section of the pipe. The bubbles travel mostly along the vertical direction without exhibiting a radial velocity component. The flow pattern is a relatively homogeneous distribution of air and water across the column which indicates that, at the given superficial velocities,

the flow is in the dispersed regime. This is consistent with the literature [6, 10, 27, 41] for similar experimental conditions.

Comparisons between simulation results obtained using case II inlet conditions and experimental data show that simulations predict the expected flow regime. Indeed, comparisons between Figures 4a and 16a and between Figures 6a and 16b show similar flow pattern. These observations support the physical relevance of the pressure Dirichlet boundary condition.

4.3. Integration of Feedback Control & Inlet Conditions

The key difficulty in enforcing the pressure boundary condition is that the velocity distribution in the inlet for the chosen value of pressure is not known *a priori*. Similarly, when using the velocity boundary condition with gas-liquid slip velocity, the slip velocity value is not available *a priori*. For both cases we propose to use a multivariable feedback control scheme that will automatically find the necessary values over time. The control procedure used along with the pressure Dirichlet boundary condition (Eqs. 8b) is described in this section. The results shown in Figs. 18-21 correspond to the flow rate configuration A. The purpose of the control is to bring the system to the desired fully-developed flow and obtain inlet values of pressure (p^{inlet}) and the gas volume fraction (α_g^{inlet}) that correspond to the desired flow rates, $Q_T^{inlet\,set}$ and $Q_g^{inlet\,set}$. The adopted control consists of two Proportional-Integral (PI) controllers (Fig. 17). The first PI controller is used to adjust Q_T^{inlet} and the second to adjust Q_g^{inlet}. In order to impose an uniform pressure boundary condition, it is necessary to compute the pressure that will correspond to a desired overall flow rate of gas and liquid. Initially, an iterative trial and error (shooting) methodology was considered whereby a pressure value was assumed and then, the velocity at the inlet was resolved from the solution of the entire problem. The goal of that preliminary procedure was to iterate on the assumed value of the pressure until the correct flow rate is obtained. However, it was found that this procedure did not converge to a solution and was computationally very intensive.

Instead, a feedback multivariable control approach was applied. With this approach, the inlet values of the pressure and the gas volume fraction were manipulated to drive the flow rates of liquid and gas to their respective set-points or desired values. The control strategy was decentralized in the sense that the flow rate of liquid was paired to the pressure and the flow rate of gas was paired to the gas volume fraction using a PI controller for each of these pairings.

Each controller in Fig. 17 generates an output signal consisting of the value of the manipulated variable in order to adjust the controlled variable to its set value. This action is performed by correcting the manipulated variable to reduce the computed error that is equal to the difference between the computed and the set values of the controlled variable. The type of control used in this work, PI control, is a simpler version of the most common control algorithm, the Proportional-Integral-Derivative (PID) control.

In the PI controller 1 (Fig. 17), the pressure p^{inlet} is manipulated to control the total volumetric flow rate Q_T^{inlet} as follows

$$\begin{aligned} \frac{\mathrm{d}p^{inlet}}{\mathrm{d}t} &= \kappa_1 \frac{\mathrm{d}E_T}{\mathrm{d}t} + \left(\frac{\kappa_1}{\tau_1}\right) E_T, \\ E_T &= Q_T^{inlet} - Q_T^{inlet\,set}, \end{aligned} \qquad \text{on inlet,} \tag{16}$$

where κ_1 is the proportional gain, τ_1 the integral time and E_T the error which represents the difference between the computed and the set total flow rates. The first term on the right hand side of the first equation of Eqs. 16 corresponds to the proportional action of the controller and the second term corresponds to the integral action where the latter term ensures that the error at fully-developed flow interval is zero. The control operated here does not include a derivative action since, for the considered problem, the resulting response with derivative action was oscillatory due to the presence of numerical noise.

In the same manner, the gas volume fraction at the inlet α_g^{inlet} is manipulated in the PI controller 2 to adjust the gas flow rate Q_g^{inlet}. The PI controller 2 is given by

$$\begin{aligned} \frac{\mathrm{d}\alpha_g^{inlet}}{\mathrm{d}t} &= \kappa_2 \frac{\mathrm{d}E_g}{\mathrm{d}t} + \left(\frac{\kappa_2}{\tau_2}\right) E_g, \\ E_g &= Q_g^{inlet} - Q_g^{inlet\,set}, \\ \alpha_l^{inlet} &= 1 - \alpha_g^{inlet}, \end{aligned} \qquad \text{on inlet,} \tag{17}$$

where κ_2 and τ_2 are the proportional gain and the integral time, respectively and E_g is the control error of the PI controller 2 and represents the difference between the computed gas flow rate and the set one.

The setting of the control parameters κ_1, τ_1, κ_2 and τ_2 is important for the efficiency and stability of the control process. In addition, each parameter has to be readjusted frequently when one or multiple inputs of the problem are

varied. This situation will be often encountered during design optimization process where the geometry, the operating flow rates and even the physical properties of the fluids are varied after each optimization iteration. Thus, readjusting the proportional gain and the integral time manually to perform stable simulations may be a tedious task. This motivated the need for using an online Estimator to set the values of κ_1 and τ_1 automatically for each simulation. It should be emphasized that a self-tuning procedure was adopted only for the PI controller 1 since for the second PI controller, rapid convergence of the controlled variable was always observed.

For the purpose of developing the online Estimator, it was assumed for simplicity that the process under consideration is of first order. Accordingly, the dependence between the controlled and the manipulated variables is given by

$$\tau_p \frac{\mathrm{d}\delta Q_T^{inlet}}{\mathrm{d}t} + \delta Q_T^{inlet} = \kappa_p \delta p_{inlet}, \tag{18a}$$

where κ_p and τ_p are the gain and the time constant of the process, respectively and $\delta Q_T^{inlet} = Q_T^{inlet} - \overline{Q}_T^{inlet}$ and $\delta p^{inlet} = p^{inlet} - \overline{p}_{inlet}$ are deviation quantities with respect to the reference values of flow rate and pressure, $\overline{Q}_T^{inlet}$ and $\overline{p}_{inlet}$. It must be mentioned that the reference quantities are estimated from the fully-developed flow solution of the simulation with inlet velocity Dirichlet boundary condition without gas-liquid slip velocity (Eqs. 8a). From Eq. 18a, the predicted flow rate is given by

$$\delta Q_T^{inlet\,pred} = \begin{bmatrix} \delta p^{inlet} & -\frac{\mathrm{d}\delta Q_T^{inlet}}{\mathrm{d}t} \end{bmatrix} \begin{bmatrix} \kappa_p \\ \tau_p \end{bmatrix}, \tag{18b}$$

Finally, the adaptation law, implemented by the Estimator block in the block diagram of Fig. 17, is defined as follows

$$\begin{bmatrix} \frac{\mathrm{d}\kappa_1}{\mathrm{d}t} \\ \frac{\mathrm{d}\tau_1}{\mathrm{d}t} \end{bmatrix} = -R \begin{bmatrix} \delta p^{inlet} \\ -\frac{\mathrm{d}Q_T^{inlet}}{\mathrm{d}t} \end{bmatrix} \left(\delta Q_T^{inlet\,pred} - \delta Q_T^{inlet} \right), \tag{18c}$$

where R is the adaptation rate of the self-tuning. With this procedure, values of κ_p and τ_p are iteratively updated using those of κ_1 and τ_1 until convergence. To ensure stability by impeding the gains from changing sign, a lower bound of 10^{-9} was imposed for both κ_1 and τ_1. In addition, to add robustness with respect to model error since the process under consideration is in reality not

first order, a dead zone of $\pm 0.1 Q_T^{inlet\,set}$ was implemented within which the self-tuning Estimator was turned off. It is given by

$$R = R_p, \qquad \left|Q_T^{inlet}\right| > 0.1\left|Q_T^{inlet\,set}\right|, \tag{18d}$$

$$R = 0, \qquad \left|Q_T^{inlet}\right| \leq 0.1\left|Q_T^{inlet\,set}\right|, \tag{18e}$$

where $R_p = 10^{-8}$ is the prescribed value of the adaptation rate.

4.3.1. Closed Loop Simulation

In this section, the performance of the control used along with the inlet pressure Dirichlet boundary condition (Eqs. 8b) is analyzed. The performance of PI controller 1 (see Fig. 17) and its online Estimator are discussed first. The performance of this controller is reported on Figs. 18 and 19. Analysis of Figs. 18 and 19 show that the PI controller 1 successfully drove the flow rate to the target total flow rate. In fact, the pressure (Fig. 18a) converged to a fully-developed flow value and the total flow rate also converged to the prescribed target at fully-developed flow interval (Fig. 18b). In addition, the self-tuning procedure was also stable as shown by the convergence of the proportional gain and the time integral respectively to constant values (see Fig. 19). Performance of the PI controller 2 is shown in Fig. 20. As observed before for the first controller, the manipulated and the controlled variables converged as $\alpha_g^{inlet}(t)$ and $Q_g^{inlet}(t)$ converged to fully-developed flow values after $t \approx 300$ s. Fig. 20b shows that the gas flow rate converged to the desired one. On the other hand, from Fig. 20a, the gas volume fraction converged to $\alpha_g^{inlet} \approx 0.035 < (Q_g^{set}/Q_T^{set})$ corroborating the occurrence of a slip velocity between the gas and liquid phases.

4.3.2. Open Loop Simulation

Analysis of the performance of the two PI controllers showed that the control strategy successfully brought the system to the desired operating flow rates and maintained the controlled variables at their target. However, it was of interest to test the stability of the process when it is operated in open-loop without the controller. This is important since it should be remembered that the feedback control was artificially introduced only to enforce an inlet pressure that corresponds to a particular flow rate. Thus, the open-loop stability of the simulation was checked and the closed and open-loop solutions were compared to check whether, after reaching the desired flow and corresponding pressure or slip velocity values, the simulations remain stable even after the controller is removed.

It was found that the open-loop simulation, for the same air and water flow rates considered for the closed-loop simulation, was unstable. The open-loop instability is due to relatively low viscous dissipation in the flow and to the appearance of backflow at the inlet boundary that progressively brings the system to instability. The origin of the instability was confirmed by performing stable open-loop simulations by augmenting the viscous dissipation using a liquid of higher viscosity than water that resulted in stability.

Moreover, it was also found from experimenting with different initial conditions that multiple solutions to the considered two-phase flow problem exist. These solutions correspond to infinite possible distributions of the two phases over the computational domain. For the uniform pressure Dirichlet boundary condition, it was found that when two-phase columns of dispersion of higher total density than the average one form in the pipe, they give rise to backflow at locations where the uniformly imposed inlet pressure was unable to compensate for dispersion. This backflow results in transient high velocity gradients and numerical instability.

One alternative to stabilize the flow simulations without explicitly using feedback control is to assess the stability of the process when the pipe is considered together with the pump that is driving the flow. This was motivated by the observation that the calculated backflow into the pump exit chamber will surely affect the pressure value there. Following this reasoning, an additional physical constraint was imposed at the inlet boundary. This constraint was inspired from the centrifugal pump characteristic curve at fixed rotation speed. It is given by

$$\left(\Delta p_{outlet}^{inlet}\right)\left(Q_T^{inlet}\right) = C, \tag{19}$$

where $C = \left(\overline{\Delta p_{outlet}^{inlet}}\right)\left(\overline{Q_T^{inlet}}\right)$ is a constant computed from the closed-loop simulation from time-averages of the pressure and total flow rate over the fully-developed flow interval (FDFI). The constraint described by Eq. 19 states that at FDFI, for a given inlet$-$outlet pressure difference, corresponds a unique total volumetric flow rate. The results of the open-loop simulation with the additional constraint of Eq. 19 were reported on Fig. 21. Indeed, the analysis of these figures show that the open-loop simulation is stable over the investigated time interval. Fig. 21a shows that the value of p^{inlet} is comparable to that obtained when fully-developed flow is reached in the closed-loop simulation (Fig. 18a). Figs. 21b and 21c show that the total and gas flow rates correspond to the set values. Thus, imposing a physically motivated constraint related to the pump can be effectively used to stabilize

the simulations at the desired values of volumetric flows and inlet pressure values without explicitly using feedback control.

5. Conclusions

The two-phase upward dispersed co-current flow of air and water in a vertical cylindrical pipe under isothermal conditions was considered. The flow problem, modeled by the two-fluid model, was solved numerically and particular attention was paid to the choice of the inlet boundary conditions. Specifically, their impact on the solutions of two-phase Eulerian flow problems was investigated.

While a uniform pressure Dirichlet boundary condition was used on the outlet boundary, three different boundary conditions were considered on the inlet and their effect on the resulting flow was analyzed. These three inlet boundary conditions are:

- The simple to implement, widely used, but physically inconsistent, uniform velocity Dirichlet boundary condition violates the no-slip condition at the wall and ignore the slip velocity between the phases at the inlet boundary.
- The uniform pressure Dirichlet boundary condition, that is considered physically consistent as the pressure fields across the cross section areas of the pipe are uniform. In addition, using this boundary condition, the no-slip condition at the wall and gas-liquid slip velocity at the inlet are no longer violated.
- The velocity Dirichlet boundary condition with slip between the two phases where the gas-liquid slip velocity is estimated from the pressure Dirichlet boundary condition simulation. Although not strictly physical, it was investigated in order to determine whether by considering the correct inlet slip velocity between the phases, it is possible to obtain a flow pattern similar to the one obtained with pressure Dirichlet boundary condition.

The different flow profiles resulting from the simulations using each one of the inlet boundary conditions were thoroughly analyzed. It was found that the choice of the relevant inlet boundary conditions for two-phase flow problems is crucial. The analysis revealed that the solution obtained with velocity Dirichlet boundary conditions is radically different from that resulting

from the use of pressure Dirichlet boundary condition even when the correct gas-liquid slip velocity was considered.

In fact, unlike what it is frequently stated in the literature, the distribution of the phases in the fully-developed flow over the considered domain is significantly affected by the inlet boundary condition and remains sensitive to it even far from the inlet boundary. Whereas the flow resulting from the velocity Dirichlet boundary condition without gas-liquid slip velocity is in the form of gas-rich rising columns, the one obtained with the pressure Dirichlet boundary condition is in the form of a homogeneous dispersion. Moreover, considering the correct gas-liquid slip velocity with the velocity Dirichlet boundary condition resulted in a dispersion much more homogeneous than the one obtained with pressure Dirichlet boundary condition.

The significant differences in flow patterns and phase distributions observed for the three inlet conditions cases considered in this study suggest that in the presence of additional phenomena as heat transfer or chemical reaction(s), the macroscopic quantities related to these phenomena are likely to be affected by the choice of the boundary conditions.

A multivariable feedback control procedure was proposed for enforcing the inlet pressure Dirichlet boundary condition that corresponds to a desired flow rate. It consists of two Proportional-Integral (PI) controllers with self-tuning for one of them. Finally, open-loop and closed-loop stability of the numerical simulation were discussed. It was shown that the concept of the characteristic pump curve can be used to stabilize the simulations at the desired values of volumetric flows and inlet pressure values in the absence of the PI feedback controllers.

Acknowledgements

This research was supported by the Natural Sciences and Engineering Research Council (NSERC) of Canada, Shell Canada, and Compute Canada.

References

[1] Drew, D. A., Lahey, R. T., 1987. The virtual mass and lift force on a sphere in rotating and straining inviscid flow. Int. J. Multiphase Flow 13 (1), 113 – 121.

[2] Du, W., Bao, X., Xu, J., Wei, W., 2006. Computational fluid dynamics (cfd) modeling of spouted bed: Assessment of drag coefficient correlations. Chem. Eng. Sci. 61 (5), 1401–1420.

[3] Duda, A., Koza, Z., Matyka, M., Sep. 2011. Hydraulic tortuosity in arbitrary porous media flow. Phys. Rev. E 84 (3), 036319.

[4] Ekambara, K., Sanders, R. S., Nandakumar, K., Masliyah, J. H., 2008. Cfd simulation of bubbly two-phase flow in horizontal pipes. Chem. Eng. J. 144 (2), 277–288.

[5] Enwald, H., Peirano, E., Almstedt, A.-E., 1996. Eulerian two-phase flow theory applied to fluidization. Int. J. Multiphase Flow 22, 21–66.

[6] Fair, J. R., 1967. Designing gas-sparged reactors. Chem. Eng. 74 (14), 67–74.

[7] Frank, T., Zwart, P. J., Krepper, E., Prasser, H.-M., Lucas, D., 2008. Validation of cfd models for mono-and polydisperse air–water two-phase flows in pipes. Nucl. Eng. Des. 238 (3), 647–659.

[8] Gesit, G., Nandakumar, K., Chuang, K. T., 2003. Cfd modeling of flow patterns and hydraulics of commercial-scale sieve trays. AlChE J. 49 (4), 910–924.

[9] Gregorc, J., Žun, I., 2013. Inlet conditions effect on bubble to slug flow transition in mini-channels. Chem. Eng. Sci. 102, 106–120.

[10] Hyndman, C. L., Larachi, F., Guy, C., 1997. Understanding gas-phase hydrodynamics in bubble columns: a convective model based on kinetic theory. Chem. Eng. Sci. 52 (1), 63 – 77.

[11] Ishii, M., Hibiki, T., 2011. Thermo-fluid dynamics of two-phase flow. Springer Science & Business Media.

[12] Issa, R. I., Kempf, M. H. W., 2003. Simulation of slug flow in horizontal and nearly horizontal pipes with the two-fluid model. Int. J. Multiphase Flow 29 (1), 69–95.

[13] Jakobsen, H. A., 2014. Chemical reactor modeling: multiphase reactive flows. Springer Science & Business Media.

[14] Jakobsen, H. A., Lindborg, H., Dorao, C. A., 2005. Modeling of bubble column reactors: progress and limitations. Ind. Eng. Chem. Res. 44 (14), 5107–5151.

[15] Jia, X., Wen, J., Feng, W., Yuan, Q., 2007. Local hydrodynamics modeling of a gas-liquid-solid three-phase airlift loop reactor. Ind. Eng. Chem. Res. 46 (15), 5210–5220.

[16] Jia, X., Wen, J., Zhou, H., Feng, W., Yuan, Q., 2007. Local hydrodynamics modeling of a gas–liquid–solid three-phase bubble column. AlChE J. 53 (9), 2221–2231.

[17] Jin, T., Li, Y. J., Liang, Z. B., Lan, Y. Q., Lei, G., Gao, X., 2017. Numerical prediction of flow characteristics of slush hydrogen in a horizontal pipe. Int. J. Hydrogen Energy 42 (6), 3778–3789.

[18] Joshi, J. B., 2001. Computational flow modelling and design of bubble column reactors. Chem. Eng. Sci. 56 (21), 5893–5933.

[19] Kantarci, N., Borak, F., Ulgen, K. O., 2005. Bubble column reactors. Process Biochem. 40 (7), 2263 – 2283.

[20] Kister, H., 1992. Distillation design. McGraw-Hill Professional.

[21] Lane, C. D., McKnight, C. A., Wiens, J., Reid, K., Donaldson, A. A., 2016. Parametric analysis of internal gas separation within an ebullated bed reactor. Chem. Eng. Res. Des. 105, 44–54.

[22] Liu, Y., Roy, T., Lee, D. Y., Ishii, M., Buchanan, J. R., 2013. Experimental study of non-uniform inlet conditions and three-dimensional effects of vertical air–water two-phase flow in a narrow rectangular duct. Int. J. Heat Fluid Flow 39, 173–186.

[23] Mehta, B., Chuang, K. T., Nandakumar, K., 1998. Model for liquid phase flow on sieve trays. Chem. Eng. Res. Des. 76 (7), 843–848.

[24] Munkejord, S. T., 2006. Partially-reflecting boundary conditions for transient two-phase flow. Int. J. Numer. Method. Biomed. Eng. 22 (7), 781–795.

[25] Olsen, R., 2004. Time-dependent boundary conditions for multiphase flow. Ph.D. thesis, Fakultet for ingeniørvitenskap og teknologi.

[26] Qi, N., Zhang, H., Jin, B., Zhang, K., 2011. Cfd modelling of hydrodynamics and degradation kinetics in an annular slurry photocatalytic reactor for wastewater treatment. Chem. Eng. J. 172 (1), 84–95.

[27] Schumpe, A., Grund, G., 1986. The gas disengagement technique for studying gas holdup structure in bubble columns. Can. J. Chem. Eng. 64 (6), 891–896.

[28] Shah, Y. T., Kelkar, B. G., Godbole, S. P., Deckwer, W.-D., 1982. Design parameters estimations for bubble column reactors. AIChE J. 28 (3), 353–379.

[29] Shaikh, A., Al-Dahhan, M., 2007. Review on flow regime transition in bubble columns. Int. J. Chem. React. Eng. 5, 1–70.

[30] Simonnet, M., Gentric, C., Olmos, E., Midoux, N., 2008. Cfd simulation of the flow field in a bubble column reactor: Importance of the drag force formulation to describe regime transitions. Chem. Eng. Process. 47 (9), 1726 – 1737.

[31] Sokolichin, A., Eigenberger, G., Lapin, A., 2004. Simulation of buoyancy driven bubbly flow: Established simplifications and open questions. AIChE J. 50 (1), 24 – 45.

[32] Tabib, M. V., Roy, S. A., Joshi, J. B., 2008. Cfd simulation of bubble columnan analysis of interphase forces and turbulence models. Chem. Eng. J. 139 (3), 589–614.

[33] The OpenFOAM Foundation, 2017. `OpenFOAM`: Open Source Field Operation and Manipulation Library.
URL `http://www.openfoam.org/`

[34] Tomiyama, A., Kataoka, I., Iztok, Z., Sakaguchi, T., 1998. Drag coefficients of single bubbles under normal and micro gravity conditions. JSME Int J., Ser. B 41 (2), 472–479.

[35] Tomiyama, A., Tamai, H., Zun, I., Hosokawa, S., 2002. Transverse migration of single bubbles in simple shear flows. Chem. Eng. Sci. 57 (11), 1849 – 1858.

[36] Wang, Y., Chen, J., Larachi, F., 2013. Modelling and simulation of trickle-bed reactors using computational fluid dynamics: A state-of-the-art review. Can. J. Chem. Eng. 91 (1), 136–180.

[37] Weller, H. G., 2005. Derivation, modelling and solution of the conditionally averaged two-phase flow equations. Nabla Ltd, No Technical Report TR/HGW/02.

[38] Yoneda, K., Yasuo, A., Okawa, T., 2002. Flow structure and bubble characteristics of steam–water two-phase flow in a large-diameter pipe. Nucl. Eng. Des. 217 (3), 267–281.

[39] Yu, Y., Kim, S. D., 1991. Bubble properties and local liquid velocity in the radial direction of cocurrent gasliquid flow. Chem. Eng. Sci. 46 (1), 313 – 320.

[40] Zhang, D., Deen, N. G., Kuipers, J. A. M., 2006. Numerical simulation of the dynamic flow behavior in a bubble column: a study of closures for turbulence and interface forces. Chem. Eng. Sci. 61 (23), 7593–7608.

[41] Zhang, J.-P., Grace, J. R., Epstein, N., Lim, K. S., 1997. Flow regime identification in gas-liquid flow and three-phase fluidized beds. Chem. Eng. Sci. 52 (21), 3979 – 3992.

[42] Zhang, Y., Chao, Z., Jakobsen, H. A., 2017. Modelling and simulation of chemical looping combustion process in a double loop circulating fluidized bed reactor. Chem. Eng. J. 320, 271–282.

[43] Zhang, Y., Chao, Z., Jakobsen, H. A., 2017. Modelling and simulation of hydrodynamics in double loop circulating fluidizedbed reactor for chemical looping combustion process. Powder Technol.

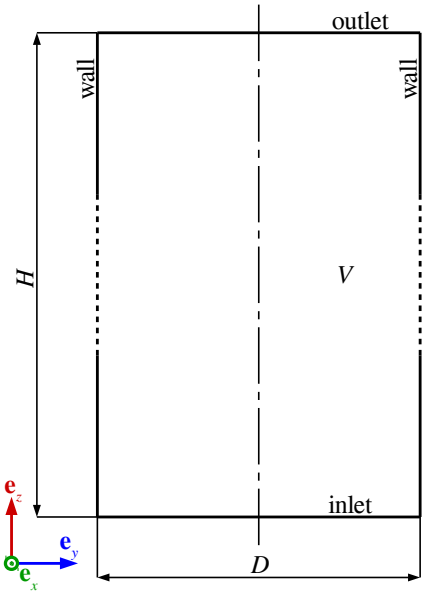

Figure 1: Schematic of the longitudinal cross-section of the three-dimensional simulation domain, a pipe of height $H = 1.5$ m, diameter $D = 15$ cm and volume V.

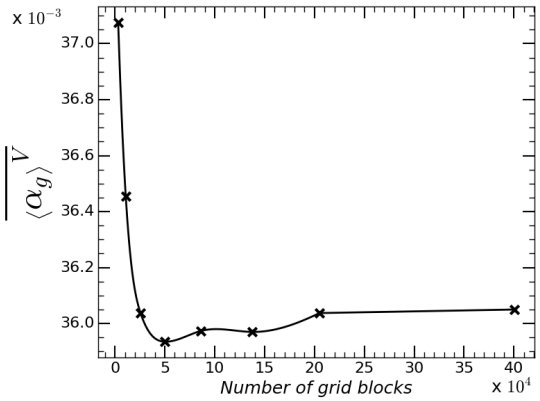

Figure 2: Gas hold up $\overline{\langle \alpha_g \rangle}^V$ (Eq. 10) versus number of mesh elements for case I inlet conditions. Configuration A: total volumetric flow rate $Q_T^{inlet\,set} = 6 \times 10^{-4}$ m^3/s and gas flow rate $Q_g^{inlet\,set} = 0.3 \times Q_T^{inlet\,set} = 1.8 \times 10^{-4}$ m^3/s.

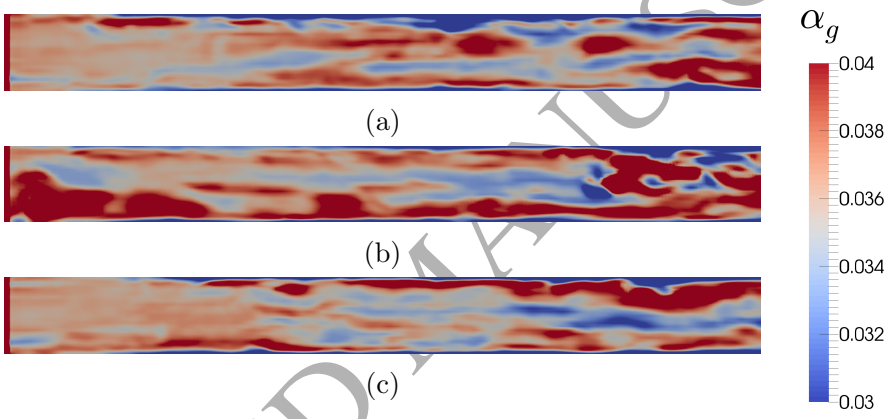

Figure 3: Simulation results of the fully-developed flow. Gas volume fraction α_g field for case I inlet conditions with (a) $t = 900$ s, (b) $t = 950$ s, and (c) $t = 1000$ s. Configuration A: total volumetric flow rate $Q_T^{inlet\,set} = 6 \times 10^{-4}$ m^3/s and gas flow rate $Q_g^{inlet\,set} = 0.3 \times Q_T^{inlet\,set} = 1.8 \times 10^{-4}$ m^3/s.

Figure 4: Simulation results of the fully-developed flow. Gas volume fraction α_g field at ($t = 1000$ s) for (a) case II and (b) case III inlet conditions. Configuration A: total volumetric flow rate $Q_T^{inlet\,set} = 6 \times 10^{-4}$ m^3/s and gas flow rate $Q_g^{inlet\,set} = 0.3 \times Q_T^{inlet\,set} = 1.8 \times 10^{-4}$ m^3/s.

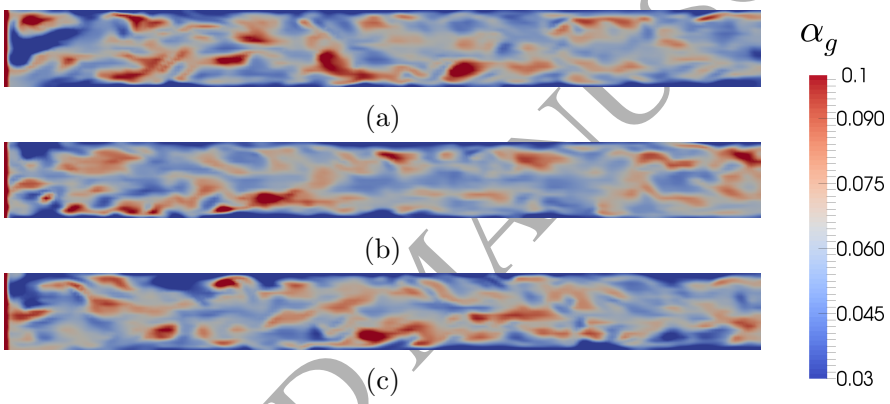

Figure 5: Simulation results of the fully-developed flow. Gas volume fraction α_g field for case I inlet conditions with (a) $t = 900$ s, (b) $t = 950$ s, and (c) $t = 1000$ s. Configuration B: total volumetric flow rate $Q_T^{inlet\,set} = 6 \times 10^{-4}$ m^3/s and gas flow rate $Q_g^{inlet\,set} = 0.5 \times Q_T^{inlet\,set} = 3 \times 10^{-4}$ m^3/s.

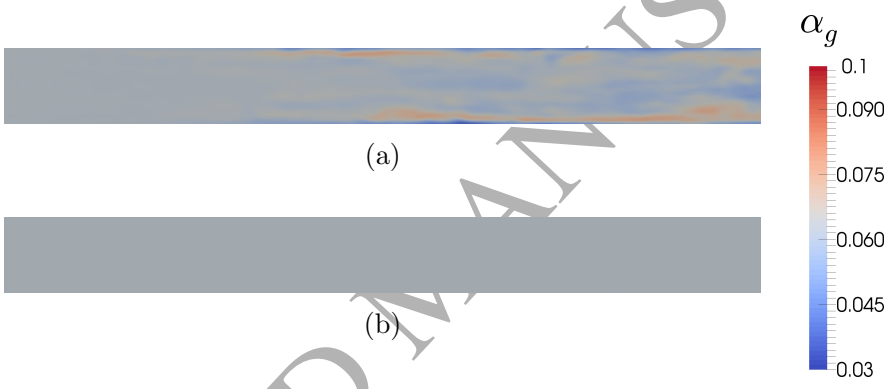

Figure 6: Simulation results of the fully-developed flow. Gas volume fraction α_g field at ($t = 1000$ s) for (a) case II and (b) case III inlet conditions. Configuration B: total volumetric flow rate $Q_T^{inlet\,set} = 6 \times 10^{-4}$ m^3/s and gas flow rate $Q_g^{inlet\,set} = 0.5 \times Q_T^{inlet\,set} = 3 \times 10^{-4}$ m^3/s.

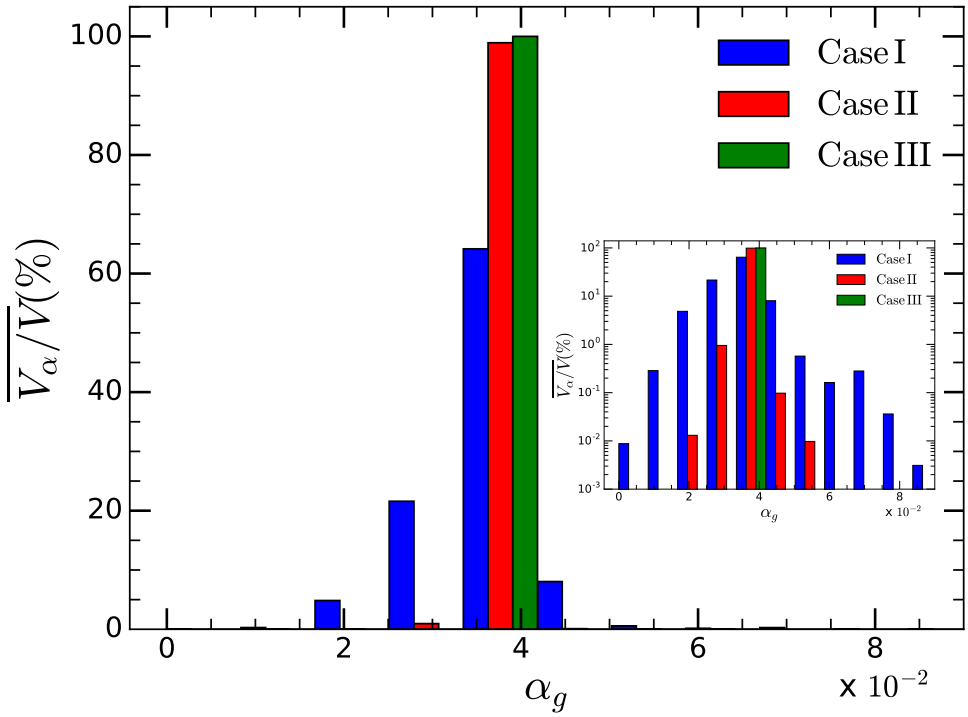

Figure 7: Histogram of time-averaged portions of the computational domain over the fully-developed flow interval (FDFI) $\overline{V_\alpha/V}$ (Eqs. 12 and 13) corresponding to the different gas volume fraction α_g intervals for each of the three inlet conditions cases (see legend). Configuration A: total volumetric flow rate $Q_T^{inlet\,set} = 6 \times 10^{-4}$ m^3/s and gas flow rate $Q_g^{inlet\,set} = 0.3 \times Q_T^{inlet\,set} = 1.8 \times 10^{-4}$ m^3/s.

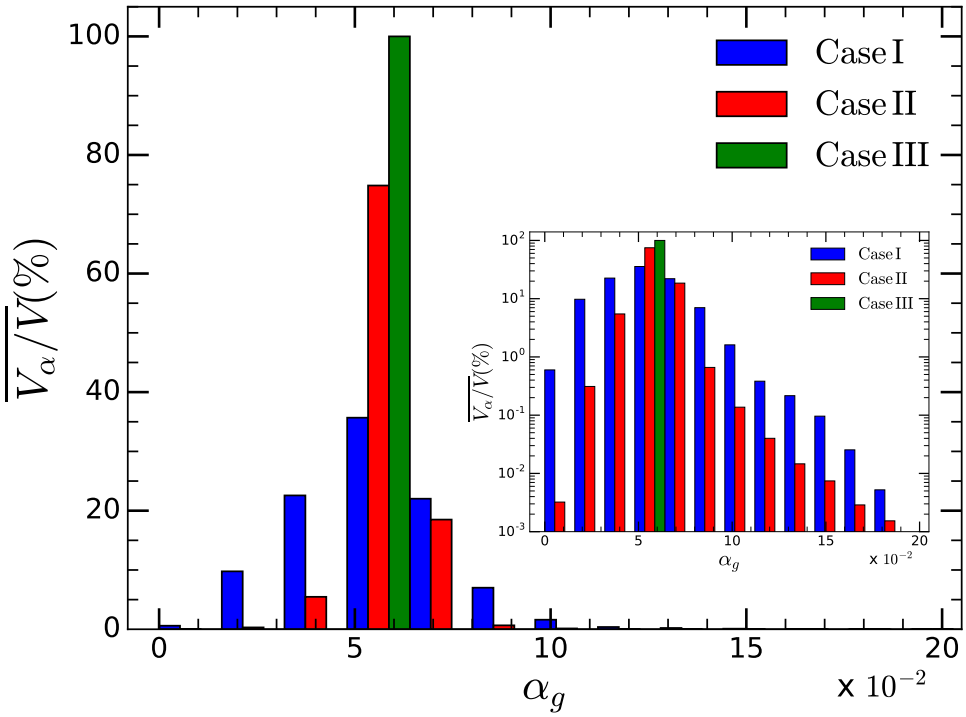

Figure 8: Histogram of time-averaged portions of the computational domain over the fully-developed flow interval (FDFI) $\overline{V_\alpha/V}$ (Eqs. 12 and 13) corresponding to the different gas volume fraction α_g intervals for each of the three inlet conditions cases (see legend). Configuration B: total volumetric flow rate $Q_T^{inlet\,set} = 6 \times 10^{-4}$ m^3/s and gas flow rate $Q_g^{inlet\,set} = 0.5 \times Q_T^{inlet\,set} = 3 \times 10^{-4}$ m^3/s.

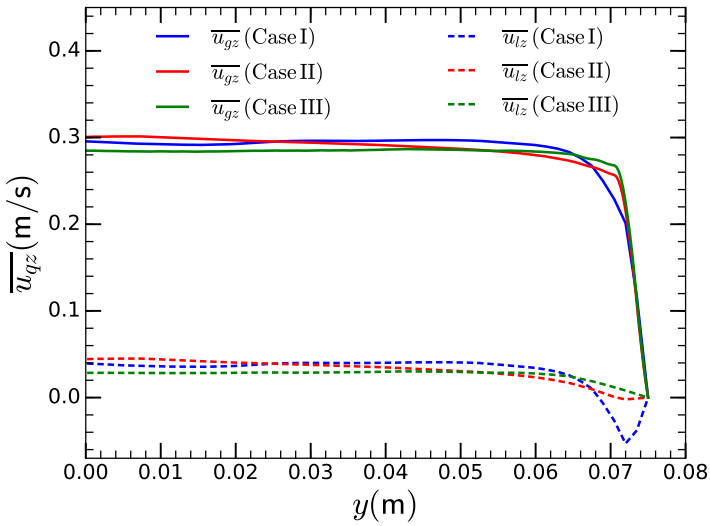

Figure 9: Simulation results of gas and liquid time-averaged velocity profiles over the fully-developed flow interval for each of the three inlet conditions cases (see legend). Profiles at half-pipe height, $z = 0.75$ m, along radial direction from the center of the pipe, $y = 0$ m, to the wall, $y = 0.075$ m. Configuration A: total volumetric flow rate $Q_T^{inlet\,set} = 6 \times 10^{-4}$ m^3/s and gas flow rate $Q_g^{inlet\,set} = 0.3 \times Q_T^{inlet\,set} = 1.8 \times 10^{-4}$ m^3/s.

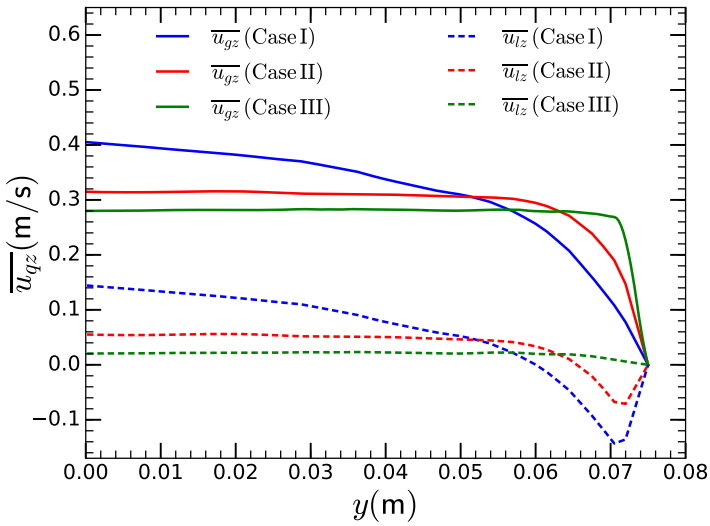

Figure 10: Simulation results of gas and liquid time-averaged velocity profiles over the fully-developed flow interval for each of the three inlet conditions cases (see legend). Profiles at half-pipe, $z = 0.75$ m, height along radial direction from the center of the pipe, $y = 0$ m, to the wall, $y = 0.075$ m. Configuration B: total volumetric flow rate $Q_T^{inlet\,set} = 6 \times 10^{-4}$ m^3/s and gas flow rate $Q_g^{inlet\,set} = 0.5 \times Q_T^{inlet\,set} = 3 \times 10^{-4}$ m^3/s.

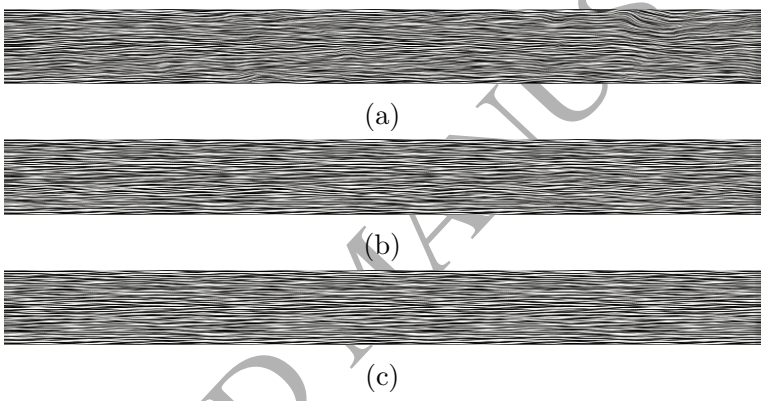

Figure 11: Simulation results of the fully-developed flow. Gas flow streamlines at (t = 1000 s) for (a) case I, (b) case II and (c) case III inlet conditions. Configuration A: total volumetric flow rate $Q_T^{inlet\,set} = 6 \times 10^{-4}$ m^3/s and gas flow rate $Q_g^{inlet\,set} = 0.3 \times Q_T^{inlet\,set} = 1.8 \times 10^{-4}$ m^3/s.

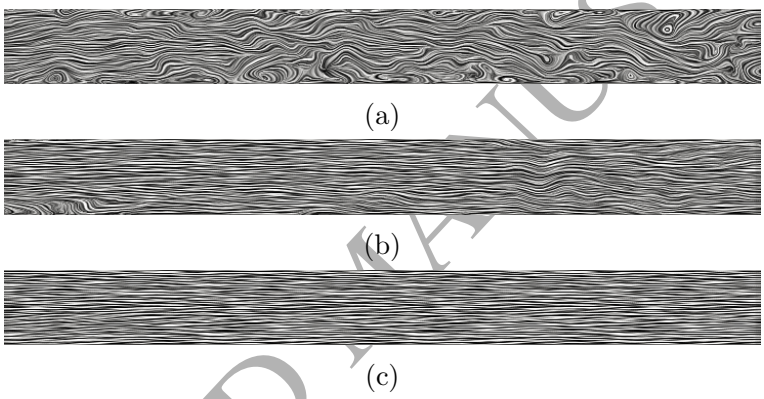

Figure 12: Simulation results of the fully-developed flow. Liquid flow streamlines at (t = 1000 s) for (a) case I, (b) case II and (c) case III inlet conditions. Configuration A: total volumetric flow rate $Q_T^{inlet\,set} = 6 \times 10^{-4}$ m^3/s and gas flow rate $Q_g^{inlet\,set} = 0.3 \times Q_T^{inlet\,set} = 1.8 \times 10^{-4}$ m^3/s.

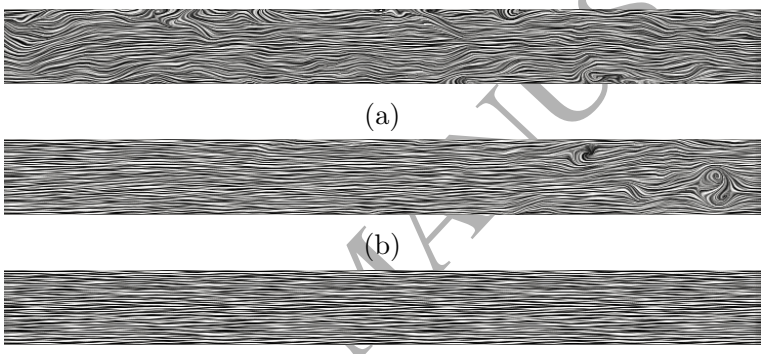

(a)

(b)

(c)

Figure 13: Simulation results of the fully-developed flow. Gas flow streamlines at (t = 1000 s) for (a) case I, (b) case II and (c) case III inlet conditions. Configuration B: total volumetric flow rate $Q_T^{inlet\,set} = 6 \times 10^{-4}$ m^3/s and gas flow rate $Q_g^{inlet\,set} = 0.5 \times Q_T^{inlet\,set} = 3 \times 10^{-4}$ m^3/s.

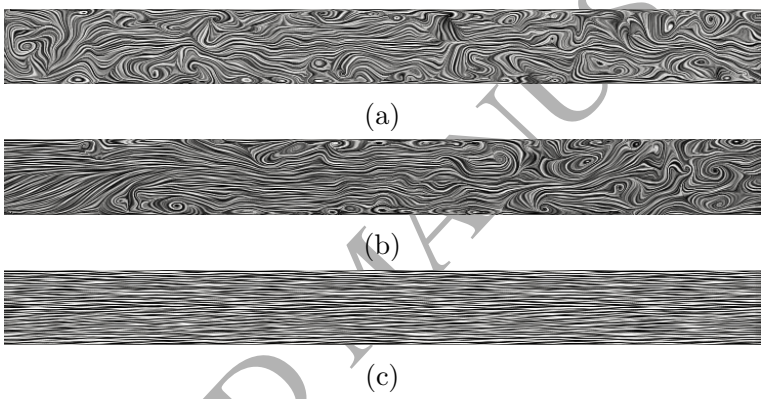

Figure 14: Simulation results of the fully-developed flow. Liquid flow streamlines at (t = 1000 s) for (a) case I, (b) case II and (c) case III inlet conditions. Configuration B: total volumetric flow rate $Q_T^{inlet\,set} = 6 \times 10^{-4}$ m^3/s and gas flow rate $Q_g^{inlet\,set} = 0.5 \times Q_T^{inlet\,set} = 3 \times 10^{-4}$ m^3/s.

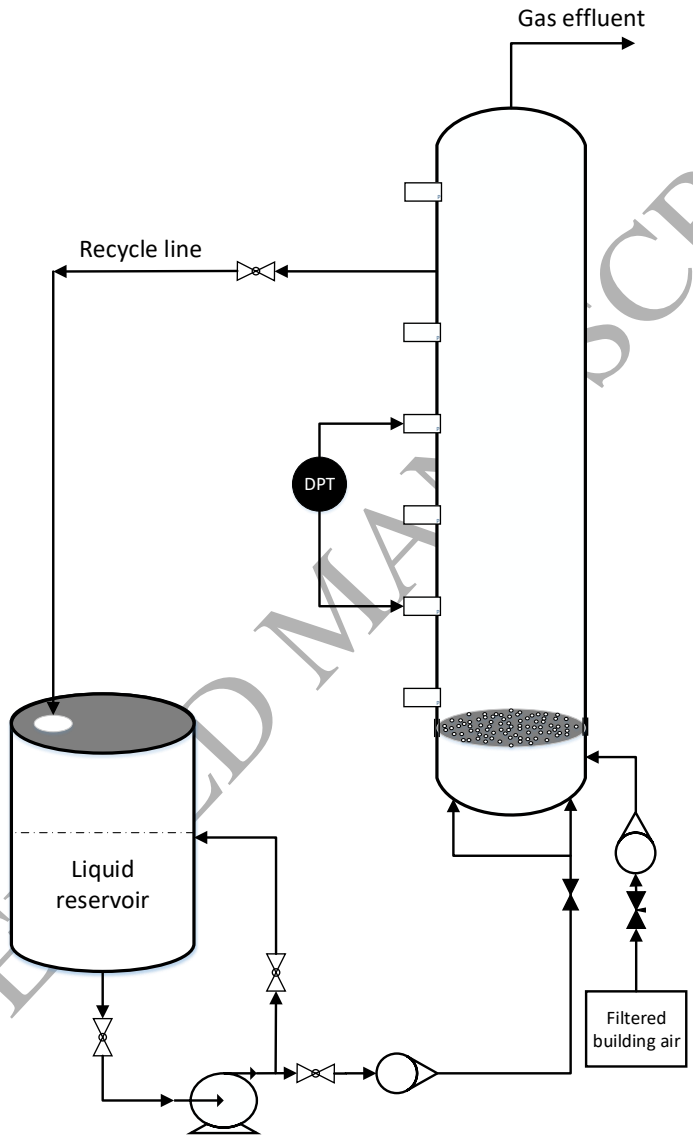

Figure 15: Schematic of the gas-liquid flow system.

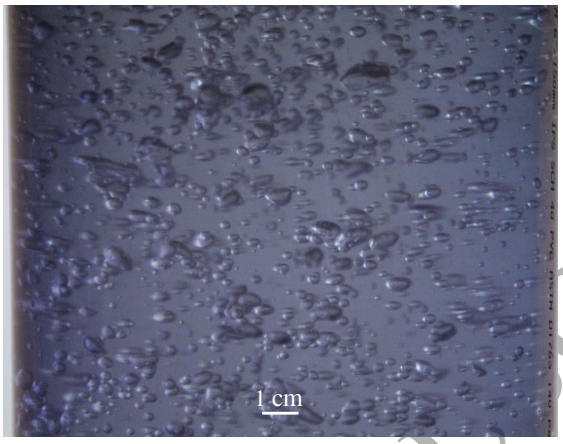

(a) Configuration A: total volumetric flow rate $Q_T^{inlet\,set} = 6 \times 10^{-4}$ m^3/s and gas flow rate $Q_g^{inlet\,set} = 0.3 \times Q_T^{inlet\,set} = 1.8 \times 10^{-4}$ m^3/s.

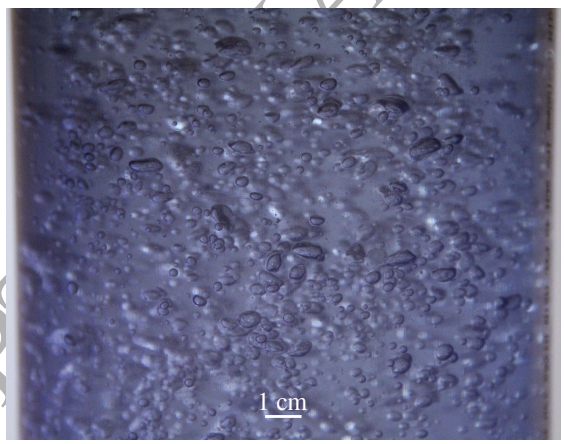

(b) Configuration B: total volumetric flow rate $Q_T^{inlet\,set} = 6 \times 10^{-4}$ m^3/s and gas flow rate $Q_g^{inlet\,set} = 0.5 \times Q_T^{inlet\,set} = 3 \times 10^{-4}$ m^3/s.

Figure 16: Observed two-phase upward flow pattern on the interval from 1.1 m to 1.3 m above the distributor plate (see Fig. 15).

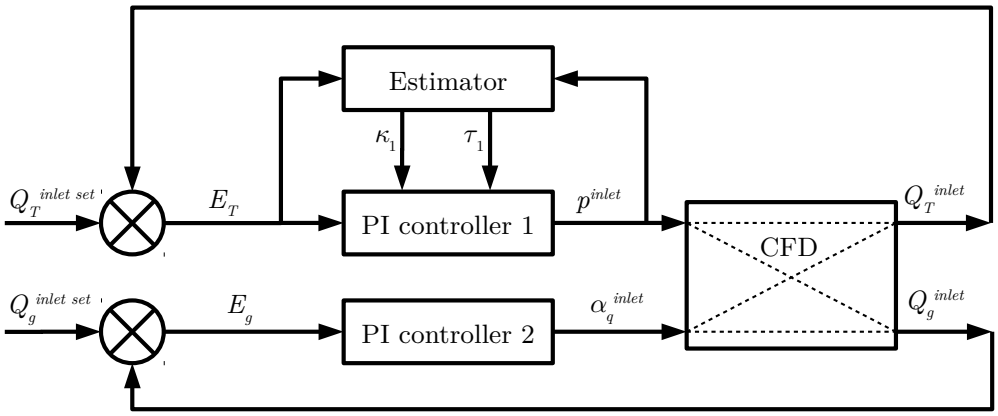

Figure 17: Multi-variable, self-tuning, Proportional-Integral (PI) control diagram used along with the Dirichlet pressure boundary condition (Eqs. 8b) at the inlet for solving the flow problem in the pipe of Fig. 1 with CFD. PI controller 1 (Eqs. 16): the pressure p^{inlet} is manipulated to control the total flow rate Q_T^{inlet} by minimizing the error $E_T = Q_T^{inlet} - Q_T^{inlet\,set}$ with respect to the set total flow rate. PI controller 2 (Eqs. 17): the gas volume fraction α_g^{inlet} is manipulated to control the gas flow rate Q_g^{inlet} by minimizing the error $E_g = Q_g^{inlet} - Q_g^{inlet\,set}$ with respect to the set gas flow rate. The Estimator (Eqs. 18) adjusts the proportional gain κ_1 and the integral time τ_1 of the PI controller 1.

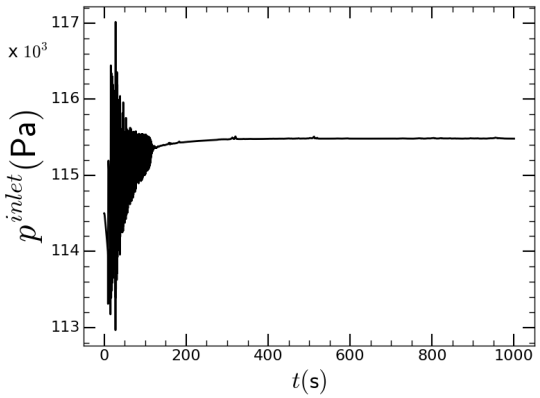

(a) The manipulated variable, value of the pressure p^{inlet}, versus time t.

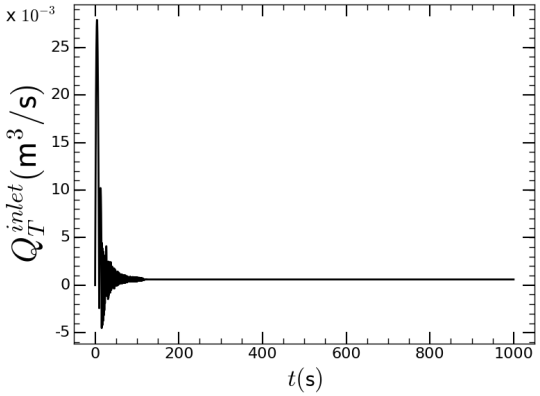

(b) The controlled variable, total volumetric flow rate Q_T^{inlet}, versus time t. Convergence to the set flow rate $Q_T^{inlet\,set}$.

Figure 18: Performance of PI controller 1 of Fig. 17. Two-phase flow of water and air in the vertical pipe of Fig. 1. Upward flow induced by case II inlet conditions, pressure Dirichlet boundary condition of Eqs. 8b. Configuration A: total volumetric flow rate $Q_T^{inlet\,set} = 6 \times 10^{-4}$ m^3/s and gas flow rate $Q_g^{inlet\,set} = 0.3 \times Q_T^{inlet\,set} = 1.8 \times 10^{-4}$ m^3/s.

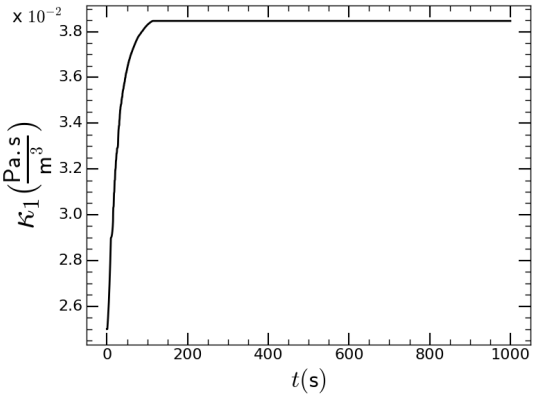

(a) Proportional gain κ_1 versus time t. Convergence to the gain of the process κ_p.

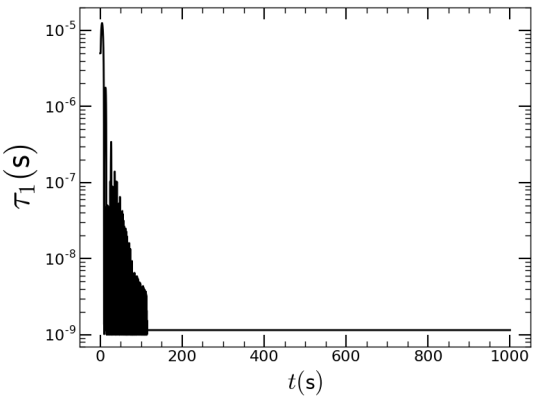

(b) Integral time τ_1 versus time t. Convergence to the time constant of the process τ_p.

Figure 19: Performance of the online Estimator used along with PI controller 1 of Fig. 17. Two-phase flow of water and air in the vertical pipe of Fig. 1. Upward flow induced by case II inlet conditions, pressure Dirichlet boundary condition of Eqs. 8b. Configuration A: total volumetric flow rate $Q_T^{inlet\,set} = 6 \times 10^{-4}$ m^3/s and gas flow rate $Q_g^{inlet\,set} = 0.3 \times Q_T^{inlet\,set} = 1.8 \times 10^{-4}$ m^3/s.

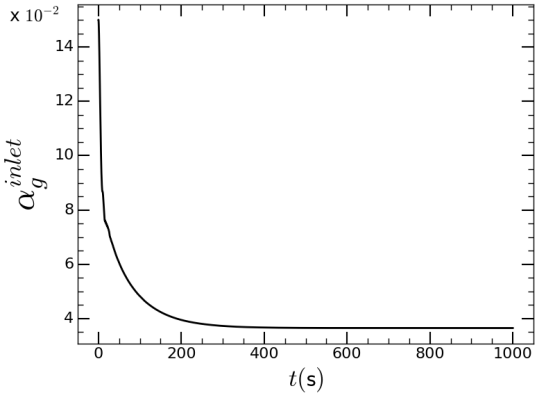

(a) The manipulated variable, value of the gas volume fraction α_g^{inlet}, versus time t.

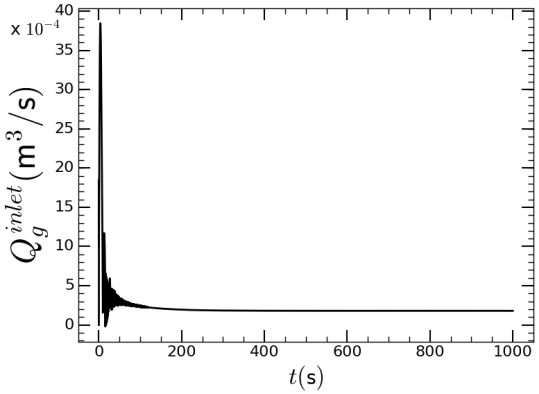

(b) The controlled variable, gas volumetric flow rate Q_g^{inlet}, versus time t. Convergence to the set gas flow rate $Q_g^{inlet\,set}$.

Figure 20: Performance of PI controller 2 of Fig. 17. Two-phase flow of water and air in the vertical pipe of Fig. 1. Upward flow induced by case II inlet conditions, pressure Dirichlet boundary condition of Eqs. 8b. Configuration A: total volumetric flow rate $Q_T^{inlet\,set} = 6 \times 10^{-4}$ m^3/s and gas flow rate $Q_g^{inlet\,set} = 0.3 \times Q_T^{inlet\,set} = 1.8 \times 10^{-4}$ m^3/s.

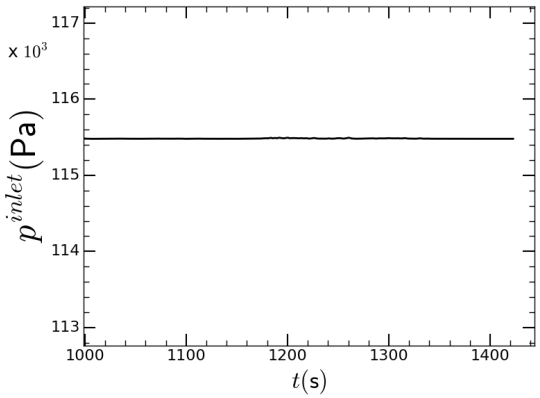

(a) Pressure p^{inlet} versus time t.

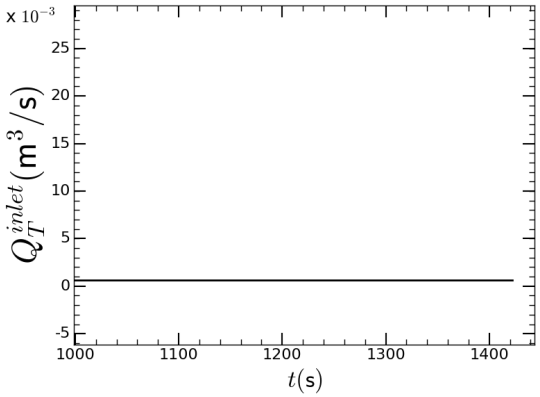

(b) Total volumetric flow rate Q_T^{inlet} versus time t.

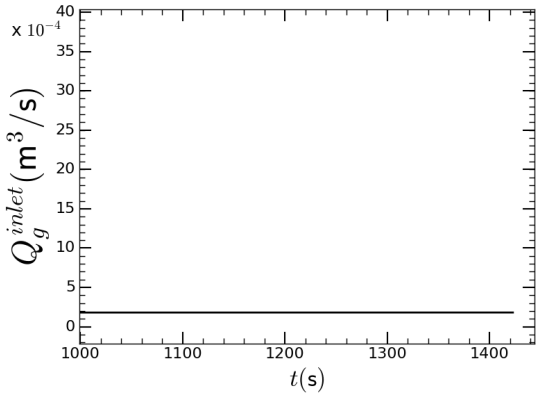

(c) Gas volumetric flow rate Q_g^{inlet} versus time t.

Figure 21: Open-loop simulation with the additional constraint of Eq. 19. Two-phase flow of water and air in the vertical pipe of Fig. 1. Upward flow induced by case II inlet conditions, pressure Dirichlet boundary condition of Eqs. 8b. Configuration A: total volumetric flow rate $Q_T^{inlet\,set} = 6 \times 10^{-4}$ m^3/s and gas flow rate $Q_g^{inlet\,set} = 0.3 \times Q_T^{inlet\,set} = 1.8 \times 10^{-4}$ m^3/s.

Table 1: Physical properties of the two fluid phases g (air) and l (water) at temperature $T = 293.15$ K and pressure $p = 101325$ Pa.

	gas (g)	liquid (l)
Density (ρ) [kg/m^3]	1.205	998.3
Kinematic viscosity (ν) [m^2/s]	15.11×10^{-6}	1.004×10^{-6}
Gas-liquid surface tension (σ) [N/m]	72.86×10^{-3}	
Bubble diameter (d) [mm]	3.000	–
Droplet diameter (d) [mm]	–	1.000

Table 2: Summary table of the time-averaged liquid flow tortuosity, $\overline{T}$, over the fully-developed flow interval (Eqs. 14 and 15) for the cases I, II and III inlet conditions and the flow rate configurations A and B.

	Case I	Case II	Case III
Configuration A	3.14	1.31	1.00
Configuration B	7.48	3.83	1.00